Soft Matter

Frustrated Crystallization Kinetics in Marginally Mismatched Binary Self-Assembly Driven by Depletion Interactions

Journal:	*Soft Matter*
Manuscript ID	SM-ART-04-2025-000433
Article Type:	Paper
Date Submitted by the Author:	29-Apr-2025
Complete List of Authors:	Tahmid Shahriar, S.; California State University Fullerton, Mechanical Engineering Feltman, Chris; California State University Fullerton, Mathematics Machler, Sean; California State University Fullerton, Physics Tanjeem, Nabila; California State University Fullerton, Physics

ARTICLE

Frustrated Crystallization Kinetics in Marginally Mismatched Binary Self-Assembly Driven by Depletion Interactions

Received
Accepted

DOI: 10.1039/x0xx00000x

Sk Tahmid Shahriar,[a] Chris Feltman,[b] Sean Machler,[c] and Nabila Tanjeem†[c]

We investigate two-dimensional crystal assemblies formed by a binary mixture of colloidal particles with a size ratio of 0.88 and driven by short-ranged depletion interactions. Our experiments show that the orientational order of the assembly decreases with an increasing fraction of impurity particles, reaching up to 18% reduction in a 1:1 binary mixture compared to a monodisperse suspension. We observe slower growth rate and arrested dynamics in the binary mixture, whereas the monodisperse sample follows a two-step nucleation and growth mechanism. We performed molecular dynamics simulations to calculate the minimum energy states for different size ratios and number ratios of the binary mixture. The simulation results predict a compromised translational order but sustained orientational order in a binary mixture with a size ratio as high as 0.88. From the combined experimental and numerical results, we conclude that the disordered assemblies found in a binary mixture originate from the frustration in assembly kinetics rather than topological frustration when there is a marginal mismatch between the two particle sizes.

1. Introduction

Studies on colloidal self-assembly are instrumental in developing fundamental insights into material phases and designing applications by leveraging the mechanical and optical properties of the assembled phases.[1–5] The simplest components of colloidal self-assembly are monodisperse particles whose size, shape, interparticle interactions, and concentration determine the properties of the assembled phases. To realize greater complexity in the phase behavior and assembly kinetics, suspensions made of two different particle sizes, i.e., binary mixtures, have been employed in numerous experimental and computational studies.[6–13] Binary assemblies are the simplest model of polydisperse colloids that are the closest approximation to colloidal suspensions found in nature and relevant for many industrial applications. Insights gained from binary assembly experiments can be applied to understand the formation of metal alloys at the atomic scale[14,15] and to design materials with the desired crystalline structure.[16–20] Therefore, interest in understanding binary colloidal self-assembly for a wide range of experimental parameters, including particle size ratios, materials, compositions, spatial confinement, and interparticle interaction potentials, is rising rapidly.

An important determinant of colloidal self-assembly is the nature of the interparticle interaction potential. While hard sphere assembly has been a common choice for studying phase behavior, assembly mechanisms that involve engineering the attractive potential between particles by tuning electrostatic, DNA-hybridization, and depletion interactions have become increasingly popular.[21–23] Specifically, self-assembly driven by depletion forces allows for tuning the strength and the range of the attractive interaction potential simply by varying the assembly components, hence it has been employed for programming the structures of colloidal clusters.[24–28] Another important aspect of depletion interaction is that its strength depends on the geometry of the particles and the nearby surfaces; this property allows the formation of two-dimensional colloidal crystals on a surface whose curvature is smaller than the particle curvature.[29,30] Therefore, depletion-induced self-assembly has been an attractive choice for investigating 2D colloidal crystallization mechanisms on flat and curved surfaces.[31,32] Such systems have a diverse set of applications involving photonic crystals,[27,33] semiconducting particle assembly,[34] chiral nanomaterials,[31,35] photonic balls,[36,37], and colloidal epitaxy.[10,38] Despite significant interest, it is yet unknown how depletion-driven 2D colloidal crystallization is affected by particle polydispersity, the simplest case of which is a binary system comprised of two different particle sizes.

[a] Department of Mechanical Engineering, California State University, Fullerton, Fullerton, California, 92831, United States.
[b] Department of Mathematics, California State University, Fullerton, Fullerton, California, 92831, United States.
[c] Department of Physics, California State University, Fullerton, Fullerton, California, 92831, United States.
† Corresponding author
Supplementary Information available: [details of any supplementary information available should be included here]. See DOI: 10.1039/x0xx00000x

Here, we investigate two-dimensional binary colloidal self-assembly driven by a short-ranged depletion interaction potential, where the ratio of the small particle diameter to the large particle diameter is $\frac{d_1}{d_2} = 0.88$, and the range of the attractive interaction potential is only 4% of the particle diameter. Prior work on binary colloidal self-assembly in the presence of depletion interactions investigated the phase behavior in bulk,[39–41] observed eutectic crystallization,[42,43] and the formation of colloidal gels.[44,45] Toyotama et al. found phase-separated eutectic crystals for a size ratio of particles (0.83) that was closer to our system but driven by a long-ranged interaction potential (80% of particle diameter). Pandey et al. investigated self-assembly with short-ranged depletion interaction (4% of particle diameter) in a binary mixture of particles with a size ratio of 0.49 and observed the formation of 3D colloidal gels and arrested particle dynamics. To our knowledge, no experiments have explained the formation of 2D binary crystals driven by short-ranged depletion interactions, especially in the presence of a small asymmetry in the particle sizes. Therefore, we performed a combination of experimental and computational investigation to elucidate how the size ratio and the relative concentrations of the two particle species determine the structural order and the assembly kinetics.

We found that the orientational hexatic order parameter of the self-assembled binary monolayer reduces by 18% in a 1:1 binary mixture compared to a monodisperse suspension. Additionally, the binary mixture exhibits much slower growth kinetics that is accompanied by cooperative particle motion. To explain the experimental findings, we developed a molecular dynamics simulation model to identify the minimum energy states of a 2D binary assembly driven by a short-range attractive interaction potential. The model shows that for a mixture with a greater particle size difference, i.e., $\frac{d_1}{d_2} \leq 0.86$, the hexatic order parameter decreases with an increasing fraction of impurity particles and reaches the minimum value for the 1:1 mixture. However, for a binary mixture where the particle sizes are much closer, i.e., $\frac{d_1}{d_2} = 0.88$, the orientational hexatic order parameter in the 1:1 mixture ratio sample remains the same as the sample with minimal impurity. However, in this case, a reduction in the translational order, as characterized by the average bond length, is observed. The disagreement between the computational and experimental results can be attributed to the assembly kinetics that distinguish the 1:1 mixture from a monodisperse sample. Although both samples grow in amorphous states during the first part of the assembly process, the monodisperse sample starts forming stable crystallites following two-step nucleation,[30] whereas the binary sample continues to grow in the amorphous state until the assembly attains high surface coverage and the particles become dynamically arrested. Our results provide a new insight into binary assemblies in cases where the mismatch in the particle sizes is marginal — the frustration in assembly kinetics, rather than the topological frustration, is the key factor that determines the structural order of the assembly.

2. Methods

2.1 Preparation of colloidal particle mixtures

Fluorescent polymer microspheres with two different diameters, $d_1 = 700$ nm (Fluoro-Max G700, green beads purchased from Fisher Scientific Inc.) and $d_2 = 790$ nm (Fluoro-Max R800, red beads purchased from Fisher Scientific Inc.) were used to prepare the binary mixture samples. Each of the particle suspensions was washed two times before usage. During each wash cycle, a total of 1 mL particle suspension (1% solids) was centrifuged (using Eppendorf 5430) for 5 minutes at 6500 rpm, the supernatant was removed, and the particles were re-suspended in 1 mL of Milli-Q water. The particles were redispersed in the suspension through vortex-mixing for 15-20s. Once the microsphere suspensions were prepared, they were mixed with an aqueous 36.5 mM of sodium dodecyl sulfate (SDS, purchased from Sigma Aldrich) solution for the depletion-induced self-assembly experiments. A stock solution of 100 mM SDS was first prepared by mixing 288.38 mg of SDS in 10 mL of Milli-Q water. Then the SDS solution was diluted to 73 mM by mixing 36.9 µL Milli-Q water with 100 µL of the stock SDS solution. Binary mixtures with different volume ratios were prepared as described below:

Monodisperse sample: The green beads (Fluoro- Max G700) with a diameter of $d_1 = 700$ nm were used to study the self-assembly of a monodisperse suspension. Five µL of the 1% particle suspension was mixed with an equal volume of 73 mM of SDS. 1:1 binary mixture: 10 µL of 73 mM SDS solution was mixed with 5 µL of 700 nm green beads and 5 µL of 790 nm red beads. 9: 1 binary mixture: 9 µL of 700 nm green beads and 1 µL of 790 nm red beads were mixed with 10 µL of 73 mM SDS solution. 19:1 binary mixture: 19 µL of 700 nm green beads and 1 µL of 790 nm red beads were mixed with 20 µL of 73 mM SDS solution. 39:1 binary mixture: 39 µL of 700 nm green beads and 1 µL of 790 nm red beads were mixed with 40 µL of 73 mM SDS solution.

The number ratios of the two particles in a binary mixture can be calculated based on the volume ratios of the two mixtures ($\frac{V_{700}}{V_{790}}$), particle sizes (D_p), the density of the particles (ρ_b) and the fluid (ρ_f) using the following equation:

$$\text{Number of particles/mL} = \frac{6\rho_f}{\pi {D_p}^3 (\rho_f + \frac{\rho_b}{C} - \rho_b)} \quad (1)$$

2.2 Sample chamber preparation and imaging

After the colloidal particles were mixed with SDS, the solution was transferred to a sample chamber for observation under a microscope. A 2-D sample cell was prepared by making a sandwich of a 24x50mm cover glass (purchased from VWR, no. 1) and a 22x22mm cover glass (purchased from VWR, no. 1). First, both cover glasses were pretreated in a UVO Cleaner (Jelight Model 30) for 5 minutes. A thin plastic film spacer and a 22x22mm micro cover glass were placed on top of the 24x50mm cover glass, and the corners of the chamber were sealed by applying the optical adhesive NOA 61

(Norland). The sample cell was then re-treated in the UVO Cleaner again for a minute. The particle suspension (10 μL) was injected into the thin gap between the two cover glasses. Finally, the sample cell was completely sealed by applying a 5-minute epoxy (Devcon).

The sample cells were imaged using an optical microscope immediately after sealing them. The imaging was performed using an inverted Olympus ix83 microscope equipped with a 100x (N.A. = 1.45) objective lens. Images were captured using the open-source software Fiji and its plug-in Micro-Manager 2.0. The green particles were captured using a 470 nm/525 nm (excitation/emission) filter set, and the red particles were captured using a 560 nm/ 630 nm filter set.

Below we summarize the expected number ratios of the two particles in the mixture ($\frac{N_{700}}{N_{790}}$) calculated using equation (1), and the observed number ratio measured from the self-assembled monolayers.

Table 1:

Volume ratio ($\frac{V_{700}}{V_{790}}$)	Estimated number ratio ($\frac{N_{700}}{N_{790}}$)	Observed number ratio ($\frac{N_{700}}{N_{790}}$)
39	58.22	53.96 ± 6.12
19	28.36	25.00 ± 1.44
9	13.43	12.26 ± 0.49
1	1.49	1.65 ± 0.18

2.3 Image processing and analysis

2.3.1 Identification of particle positions: The images of the colloidal crystals were first converted to 8-bit images using Fiji. An open-source Python package - Trackpy, was used to identify the particles and locate their positions from the image files.[46] The particles were identified by optimizing four different parameters – particle diameter, minimum separation distance between the neighboring particles, minimum brightness of the features, and the overall brightness profile. The estimated particle diameter was calculated from the microscopic images using Fiji, and the minimum separation distance was kept at a value equal or close to the particle diameter. The dynamic resolution of the particle tracking was found to be 25.3 ± 3.6 nm, calculated from the mean displacement of a few stationary particles in the sample for 10s.

2.3.2 Analysis of colloidal crystal images: Three different quantitative analysis techniques were performed to characterize the features of the colloidal crystals - Voronoi diagram, hexatic order parameter, and radial distribution function. An in-house Python script was developed to calculate the Voronoi diagrams and the average hexatic order parameter. The positions (x,y coordinates) of the particles were identified using Trackpy, and an existing Python library (Voronoi from SciPy) was used to generate the Voronoi diagrams. Another Python library (NearestNeighbors and ball tree neighbor search algorithm) was used to identify the coordinates of the six nearest neighbors of every particle. A cut-off distance was applied to exclude particles that are greater than 2D (D: particle diameter) away from the nearest neighbor list. Then, the hexatic order parameter of each particle was calculated from the following equation: $|\psi_6(k)| = \left|\frac{1}{n}\sum_{j=1}^{n} e^{i6\theta_{jk}}\right|$, where θ_{jk} is the angle between the vector $\mathbf{r}_{jk}$ that connects particle k to particle j, and the x-axis. An existing Python library (PairCorrelation) was used to calculate the radial distribution function g(r) from colloidal crystal images.

2.3.3 Analysis of particle dynamics: Particles were tracked from a series of images to quantify assembly dynamics over time. First, particle locations were identified from all relevant image frames using Trackpy, and then their positions were linked to calculate the trajectories of each particle. The process was repeated for both the red and the green particles, images of which were acquired using different fluorescent channels. Quiver plots were calculated to visualize the cooperative motion of the particles from the magnitude and the direction of their displacement vectors. To achieve this plot, the displacement vectors were calculated from the initial position and the final position of the particles identified from their trajectories.

2.3.4 Calcualtion of four − point susceptibility: χ_4 quantifies the temporal fluctuations of the fraction of mobile particles, $Q(t)$, and can be estimated from the following equation:[47]

$$\chi_4(t) = N\left[\langle Q(t)^2\rangle_t - \langle Q(t)\rangle_t{}^2\right]$$

A particle was defined as mobile if its displacement at a time interval Δt is greater than a threshold displacement $\Delta L = \frac{d}{2}$, where d is the average particle diameter. The temporal fluctuations of $Q(t)$ was calculated from 100 images captured at every 30s of time intervals.

2.4 Molecular dynamics simulation

2.4.1 Defining interaction potentials: The Lennard-Jones interaction potential was employed to emulate particles with different finite sizes and short-ranged interactions. Interaction between type 1 (small) particles:

$$U_1(r) = 4\varepsilon_1\left[\left(\frac{\sigma}{r-\Delta_1}\right)^{12} - \left(\frac{\sigma}{r-\Delta_1}\right)^{6}\right],\ r < r_C + \Delta_1 \quad (2)$$

Interaction between type 2 (large) particles:

$$U_2(r) = 4\varepsilon_2\left[\left(\frac{\sigma}{r-\Delta_2}\right)^{12} - \left(\frac{\sigma}{r-\Delta_2}\right)^{6}\right],\ r < r_C + \Delta_2 \quad (3)$$

Interaction between type 1 (small) and type 2 (large) particles:

$$U_{12}(r) = 4\bar{\varepsilon}\left[\left(\frac{\sigma}{r-\bar{\Delta}}\right)^{12} - \left(\frac{\sigma}{r-\bar{\Delta}}\right)^{6}\right],\ r < r_C + \bar{\Delta} \quad (4)$$

The finite diameters the smaller and the larger particles were represented by $\Delta_1 + \sigma$ and $\Delta_2 + \sigma$, respectively. Five different size ratios $m = 0.80, 0.82, 0.84, 0.86, 0.88$ were applied to simulate different degrees of asymmetry in particle sizes. The values of Δ_2 and $\bar{\Delta}$ were calculated for each m and for a fixed value of Δ_1 (all parameters listed in Table 1). The value of σ was calculated from the experimental estimate of the range of depletion interaction - 4% of the diameter of the smaller particles, i.e., $\frac{\sigma}{\Delta_1+\sigma} = 0.04$. Since the

ratio of the interaction strengths, $\frac{\varepsilon_1}{\varepsilon_2} = m$ is true for depletion forces, ε_2 and $\bar{\varepsilon}$ were calculated from the values of ε_1 and m. The cutoff distance r_c was chosen to be approximately $1.5\,[(\Delta_1 + \sigma) + (\Delta_2 + \sigma)]$ to reduce the computation time.

2.4.2 Initialization of the simulation region: The simulations were performed in a box with dimensions 800 x 800 x 1, and particle dynamics was limited in only x and y dimensions. N_1 number of type 1 particles (diameter $d_1 = \Delta_1 + \sigma$) and N_2 number of type 2 particles (diameter $d_2 = \Delta_2 + \sigma$) were placed in random positions of the box at the beginning of the simulation. The values of N_1 and N_2 were chosen carefully to maintain a constant total surface coverage in all simulations performed for different $\frac{N_1}{N_2}$ cases. The following equations were solved to calculate N_1 and N_2.

$$N_1\pi\left(\frac{d_1}{2}\right)^2 + N_1\pi\left(\frac{d_1}{2}\right)^2 = A \qquad (5)$$

where $A \approx 425{,}000$ is the total area covered by all particles in the simulation box, and

$$\frac{N_1}{N_2} = \frac{1}{90}, \frac{1}{9}, 1 \qquad (5)$$

are the three different number ratios that were applied in the simulations. The determined values of N_1 and N_2 are summarized in Table 2.

2.4.3 Simulated annealing: We applied Langevin dynamics to reduce the temperature of the simulation gradually from $T_i = {}^{5\varepsilon}/_{k_B}$ to $T_f = {}^{0.1\varepsilon}/_{k_B}$ over a period of 5×10^5 iterations, with the time step of each iteration, τ = 0.001 s. We confirmed that closely packed crystalline structures were found at the end of the simulation period for every set of parameters. We found that the energy reaches the minimum for all simulations that were performed for longer than 10^5 iterations (for both $\tau = 0.01$ and $\tau = 0.001$). The minimum energy value was also consistent with the one found using the conjugate gradient energy minimization on LAMMPS (Figure S1).

Table 2: Parameters related to the simulated Lennard-Jones potentials

Size ratio, $m = \frac{\Delta_1+\sigma}{\Delta_2+\sigma}$	Δ_1	Δ_2	$\bar{\Delta} = \frac{\Delta_1 + \Delta_2}{2}$	σ	$\frac{\sigma}{\Delta_1 + \sigma}$	ε_1	ε_2	$\bar{\varepsilon} = \frac{\varepsilon_1 + \varepsilon_2}{2}$
0.8	4.45	5.61	5.03	0.19	0.04	5	6.25	5.63
0.82	4.45	5.47	4.96	0.19	0.04	5	6.1	5.55
0.84	4.45	5.33	4.89	0.19	0.04	5	5.95	5.48
0.86	4.45	5.19	4.82	0.19	0.04	5	5.81	5.41
0.88	4.45	5.08	4.77	0.19	0.04	5	5.68	5.34

Table 3: The number of different particle types in the simulation box

	N_1: N_2(small: large)	N_1	N_2
$m = 0.80$	90: 1	24713	273
	9:1	21420	2381
	1:1	9808	9827
$m = 0.82$	90: 1	24727	272
	9:1	21572	2353
	1:1	10102	10077
$m = 0.84$	90: 1	24727	272
	9:1	21757	2449
	1:1	10836	10840
$m = 0.86$	90: 1	24732	273
	9:1	21769	2435
	1:1	10607	10639
$m = 0.88$	90: 1	24727	283
	9:1	21947	2459
z	1:1	10976	10984

3. Results and Discussions

First, we investigated the depletion-induced phase behavior of a monodisperse colloidal particle suspension (diameter d_1 = 700 nm, 0.5% w/w) mixed with different concentrations of the depletant, sodium dodecyl sulfate (SDS). The SDS surfactants form micelles at above the critical micelle concentration (8.2 mM) and induce attractive depletion interactions between the polystyrene spheres and the flat glass surface, as well as between the polystyrene spheres themselves.[31,48] The Asakura-Osawa depletion interaction potential between two objects can be expressed as:[49] $U_{AO}(r) = -\rho k_B T V_{ov}(r)$, where ρ is the number density of the depletant micelles and V_{ov} is the overlap of the excluded volumes. Because the overlap volume between a flat surface and a sphere is greater compared to the overlap volume between two spheres, the particles first weakly adsorb to the flat glass wall at the bottom of the sample chamber and then form closely packed structures. [30–32,48,50–52]

We find no evidence of self-assembly at SDS concentrations below 30 mM (Figure S2). The particles remain in a fluid phase with SDS concentration of 30 mM and in a fluid-crystal co-existent phase at 32 mM (Figure 1a). We observe the formation of polycrystalline monolayers that cover the entire glass surface with higher SDS concentration of 34 mM (estimated particle-particle bond energy $E_b \approx -U_{\min} \approx 5.6\, k_B T$, SI section 2) and 36.5 mM ($E_b \approx 6.1\, k_B T$). The particle-particle interaction is even stronger at 38 mM and 42 mM of SDS, resulting in gel formation. From the phase behavior, we conclude that equilibrium assembly can take place through multiple particle binding and unbinding events only when the SDS concentration is in the range of 34 - 36.5 mM. We estimated the range of the attractive interaction to be about 4.84% of particle diameter by analysing a snapshot of the assembled colloidal crystals (Figure S3). The average center-to-center distance between nearest neighbors was found to be about 734 nm, only 34 nm larger than the particle diameter (700 nm).

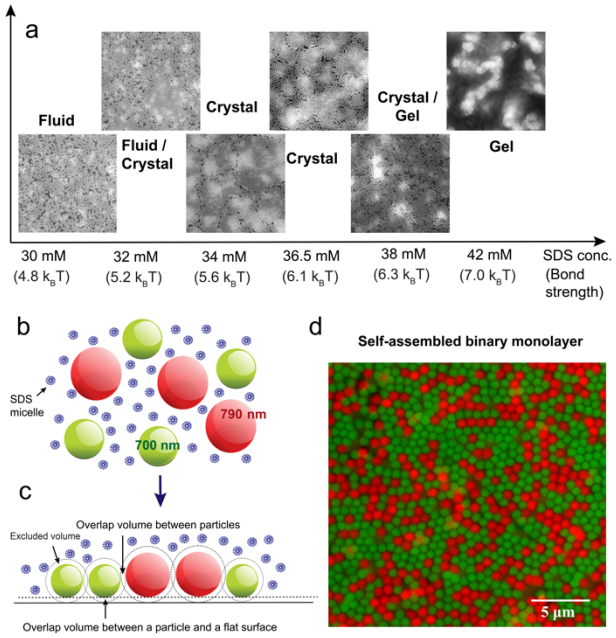

Figure 1 (a) Phase behavior of 700 nm colloidal particles when mixed with SDS at different concentrations above the CMC. The phases transitions from fluid to crystalline, then crystalline to gel with increasing SDS concentrations. (b) An illustration of the ternary mixture – the binary mixture colloidal polystyrene spheres (green: 700 nm and red: 790 nm) and the SDS micelles. (c) An illustration of the assembly mechanism driven by depletion interactions. The overlaps of the excluded volumes are shown for the particle-particle geometry and particle-flat surface geometry. A closely packed monolayer on the flat surface forms when the maximum overlap volume is achieved by minimizing the free energy of the system. (d) Optical micrograph of a self-assembled layer formed by a binary mixture of 1:1 volume ratio.

Next, we studied 2D binary assemblies by mixing 34 mM of SDS with polystyrene microspheres of two different diameters, d_1 = 700 nm and d_2 = 790 nm, (Figures 1b, 1c). The polydispersity index of the polystyrene particles was less than 3%, as reported by the supplier. Both particles, small and large, remain stable in the suspension at the applied concentration (0.5% w/w, volume fraction $\phi = 0.005$) on their own as well as when mixed with each other (Figure S4, S5). The structure and dynamics of the self-assembled monolayers were observed in real-time using an optical microscope (Olympus ix83) equipped with fluorescence imaging capabilities and a 100x oil immersion objective lens (NA = 1.45). Particles with diameter $d_1 =$ 700 nm and $d_2 = 790$ nm were identified from their fluorophore labels - green and red colors, respectively. The self-assembled monolayers formed after leaving the mixture solution in a sealed sample chamber for several hours (Figure 1d). Since the height of our sample cell (about 360 µm) was much larger than the particle diameter, we do not expect to observe any effect of the hydrodynamic interactions resulting from the spatial confinement. The observed number ratio of the two particles ($\frac{N_{700}}{N_{790}}$) in the self-assembled monolayer was found to be very close to the expected number ratio calculated from the volume ratio of the two suspensions (Table 1). The small difference could be due to the marginally stronger interaction potential between the larger particles and their lower diffusivity and higher sedimentation rate.

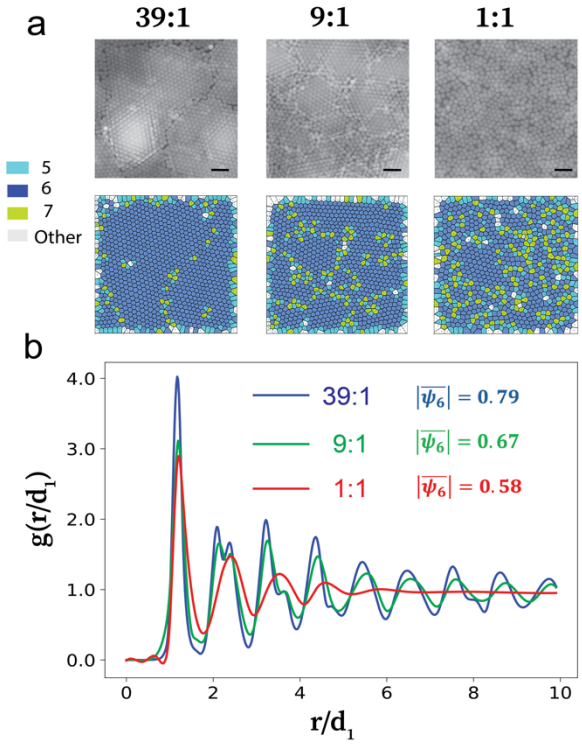

Figure 2 a) Images of crystalline and amorphous structures for different binary mixtures: 39:1, 19:1, and 1:1, and their corresponding Voronoi diagrams (scale bar 3 µm) (b) The radial distribution functions of the three mixtures shown in (a). The decline of the height of the g(r) peaks and the corresponding decrease in $|\overline{\psi_6}|$ are evident.

We investigated how the mixing ratio of the two types of particles impact the crystalline order of the formed layers. The difference in

crystalline order is evident from the corresponding Voronoi diagrams and the radial distribution function g(r), as shown in Figure 2. The 1:1 mixture (700 nm: 790 nm) sample exhibit more 5- and 7-fold defects (Figure 2a) and reduced heights in higher-order peaks compared to the 39:1 (700 nm: 790 nm) mixture sample (Figure 2b). The hexatic order parameter can be used quantify the degree of six-fold rotational symmetry around every particle, $|\psi_6(k)| = \left|\frac{1}{n}\sum_{j=1}^{n} e^{i6\theta_{jk}}\right|$. The average $|\overline{\psi_6}|$ was calculated from micrographs of particles at five different positions in a sample, each consisting of about 7500 particles, after 22 hr of observation. While the polycrystalline structures in the 39:1 mixture had a higher average hexatic order of $|\overline{\psi_6}| = 0.79$, the 1:1 mixture showed a much lower value of $|\overline{\psi_6}| = 0.58$ (distributions of $|\psi_6|$ shown in in Figure S6). The lack of crystalline order was consistently observed in samples with different particle concentrations - $|\overline{\psi_6}| = 0.51$ in a 0.13% (w/w) particle suspension and $|\overline{\psi_6}| = 0.63$ in a 0.25% (w/w) suspension (Figure S7). This result clearly indicates that the self-assembled structures transition from crystalline to amorphous for a higher fraction of impurities and thereby offers a mechanism for precise tuning of the crystalline order in 2D colloidal assemblies.

Although it may not be surprising that the addition of impurities frustrates crystalline order in binary assemblies, there are two possible mechanisms behind this frustration. The first one is a topological frustration induced by the size mismatch that would reduce the crystallinity of the equilibrium states. And the second one is a kinetic frustration induced by the specific crystal growth mechanism that restricts the assembly from reaching its equilibrium state.

To investigate the possibility of topological frustration, we developed a molecular dynamics simulation model that allows us to identify the equilibrium assembly structures for a wider range of parameters. The simulation was performed using the open-source molecular dynamics simulation package LAMMPS.[53] The different sizes of the particles were implemented by using shifted Lennard-Jones (LJ) potentials (equations 2-4), where $\Delta_1 + \sigma$ represents the diameter of the smaller particles (green) and and $\Delta_2 + \sigma$ represents the diameter of the larger particles (red).[54] The range of the attractive interaction potential was fixed at 4% of the smaller particle diameter to mimic the effective range of attractive potential (about 34 nm) [48,55] The shapes of the applied LJ potential between different particle pairs are shown in Figure 3a.

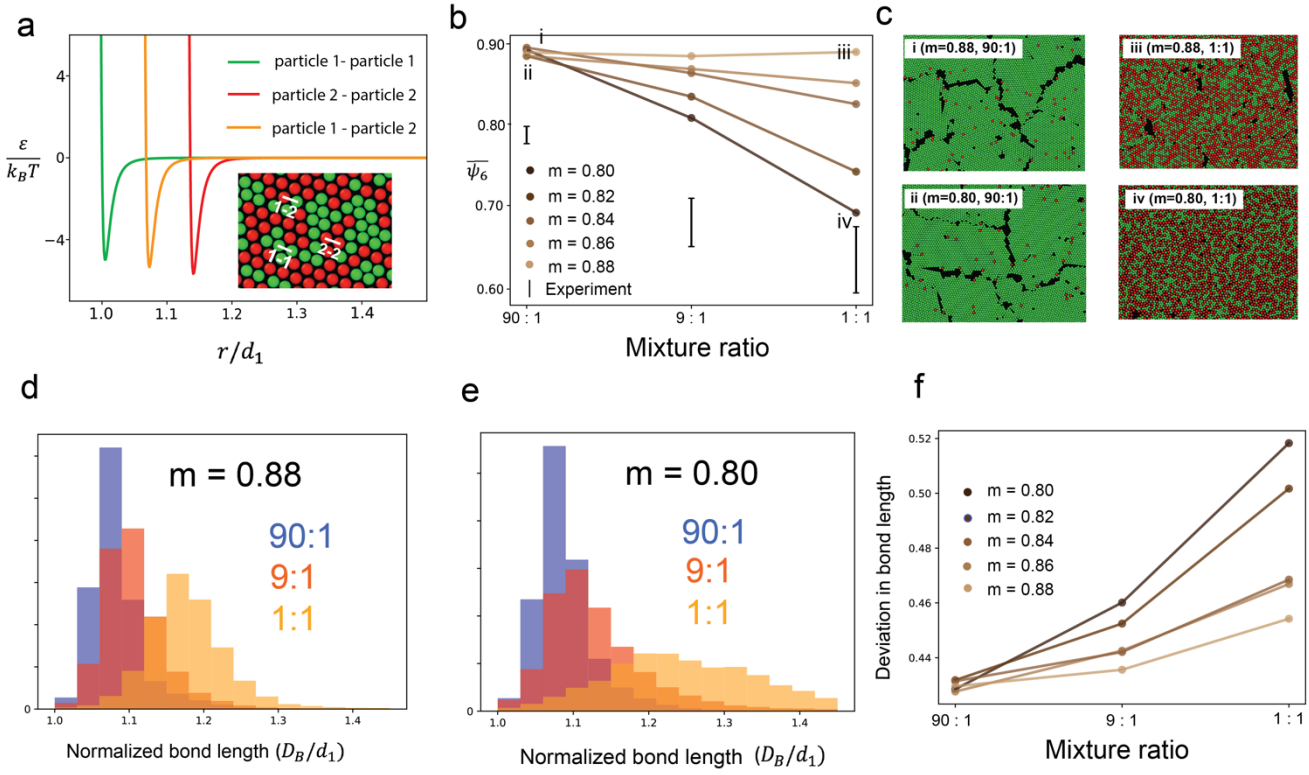

Figure 3 Simulation results (a) The Lennard-Jones interaction potentials between different particle pairs: the green line shows the interactions between the smaller particles (particle 1), the red line shows the interactions between the larger particles (particle 2), and the orange line shows the interactions between the smaller and the larger particles. (b) The average hexatic order $\overline{\psi_6}$ of the minimum energy state structures for different size ratios and number ratios, showing that the simulated orientational order decreases rapidly for the m= 0.80 sample but remains constant for the = 0.88 sample. The experimental data points were taken for $m = 0.88$. (c) The images of colloidal crystals at the ground state for four different parameter sets depicted by the data points annotated as (i), (ii), (iii) and (iv) on the plot of Figure 3b. (d) The distribution of bond lengths for $m = 0.88$ showing that the mean bond length increases with increasing fraction of impurities. (e) The distribution of bond lengths for $m = 0.80$ shows a similar trend but with a much wider distribution for the 1:1 mixture ratio. (f) The standard deviation of the bond lengths calculated from the distributions of all samples. Although smaller compared to other cases, the $m = 0.88$ sample shows a wider distribution of bond lengths as the number ratio varies from 90:1 to 1:1.

We identified the minimum energy states of the 2D assembly for different size ratios, $m = \frac{d_1}{d_2} = 0.80, 0.82, 0.84, 0.86, 0.88$ by performing simulated annealing. We observe a reduction in the average hexatic order, $|\overline{\psi_6}|$, with increasing fractions of impurities, specifically for cases where the difference in the particle sizes was larger (smaller m). For example $|\overline{\psi_6}|$ decreases from 0.89 to 0.69 as the mixture ratio varies from 90:1 to 1:1 when the simulation is performed at $m = 0.80$ (Figure 3b) However, the average hexatic order $|\overline{\psi_6}|$ does not decrease when two particle types have closely matched diameters, i.e., $m = 0.88$ – a size ratio that represents the experimental sample. The assembled structures found at the minimum energy states are shown in Figure 3c — polycrystalline structures and clearly separated grain boundaries form when the fraction of impurities is small (90:1) for both $m = 0.80$ and $m = 0.88$. In contrast, randomly distributed defects and voids are observed in the 50% mixture ratio (1:1) sample (Voronoi diagrams in Figure S8). The constant $|\overline{\psi_6}|$ value in the 1:1 and the 90:1 mixture for $m = 0.88$ indicates that the energy cost from the grain boundaries in the 90:1 mixture matches the energy cost of the voids in the 1:1 mixture. As the mismatch in particle diameters becomes larger, e.g., for $m = 0.80$, the number of defects increases, causing a significant reduction (22%) in the average hexatic order. The computational results indicate that the formation of amorphous solids in the presence of a large size mismatch can be explained primarily from the energetics of the system. This finding is consistent with prior experiments that observed glass formation in binary samples with a size ratio of 0.77 and 0.81.[47,56]

Additionally, we quantified the translational order of the assembled structures by quantifying the distributions of the center-to-center distance between neighboring particles, D_B. As shown in Figures 3d and 3e, the average $\overline{D_B}$ and the standard deviation of the distribution, δD_B gradually increases with the increasing fraction of impurities (both for $= 0.80$ and $m = 0.88$). This increase is more prominent in the presence of large size mismatch as demonstrated in Figure 3f. The finding indicates that the translational order is more sensitive to marginal mismatches in particle diameters than the orientational hexatic order. Although the asymmetric bond lengths between particle pairs reduce the average translational order, the deviation is not high enough to compromise the mean orientational order in the 1:1 binary mixture for $m = 0.88$. Therefore, the simulation results confirm that a marginal size mismatch (such as $m = 0.88$) cannot introduce enough topological frustration to reduce the hexatic order of a binary mixture sample as high as 18%.

To strengthen our conclusion, we examined the hexatic order for the $m = 0.88$ sample numerically for an even shorter range of attractive interaction – 0.22% of the particle diameter. We found that the hexatic order shows only a 2% reduction when the number ratio varies from 90:1 to 1:1 (Figure S9), much smaller compared to the 18% reduction observed in the experiment. We also examined the thermodynamic equilibrium states by exciting the ground state crystal structures with an increased temperature of k_BT. We found

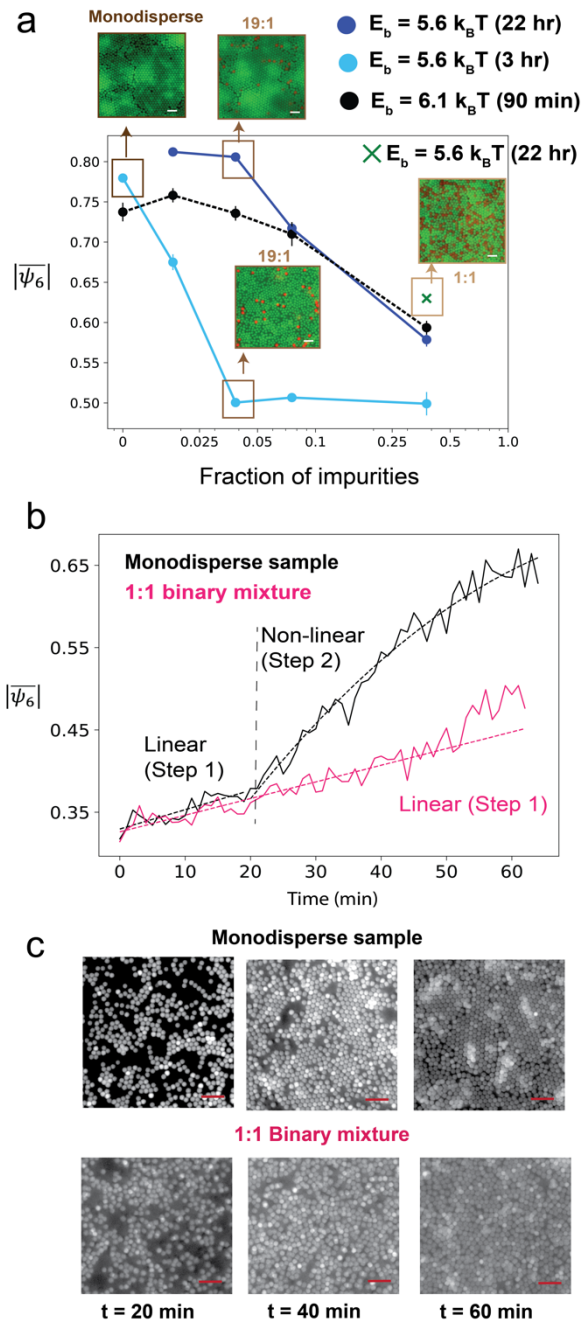

Figure 4 (a) The average hexatic order $|\overline{\psi_6}|$ decreases with the increase in impurity fractions, in samples assembled using different SDS concentrations. The impurity fraction values on the x-axis were calculated from the number ratios of the two particles observed from the crystal images. (all scale bars are 3 μm). (b) The growth curves for the monodisperse and the 1:1 binary mixture showing how $|\overline{\psi_6}|$ evolves over time. The monodisperse sample exhibits a two-step growth mechanism involving a linear growth in step 1 followed by a rapid crystallization in step 2. The binary sample follows only a linear increase in $|\overline{\psi_6}|$ during the entire observation timeframe. (c) Micrographs of the monodisperse and the 1:1 binary mixture at different time points illustrating the different crystallization kinetics. Both samples remain fluid up to the first 20 min of the assembly. Then the monodisperse sample starts forming stable crystallites at 40 min that rapidly increase in size, as observed after 60 min. In contrast, the binary mixture lacks the second nucleation step and as a result remains highly amorphous after 60 min. (scale bar 5 μm).

that the hexatic orders of all mixture ratios (90:1, 9:1, and 1:1) decrease equally from 0.89 to 0.82 at room temperature, yet any notable reduction was absent in the 1:1 sample compared to the 90:1 sample (Figure S9). Therefore, we conclude that the near equilibrium structures computed in the simulations do not explain why we observe a large reduction of $|\overline{\psi_6}|$ (18%) in the $m = 0.88$ sample when the mixture ratio changes from 90:1 to 1:1.

Therefore, we shift our focus to the investigation of the crystal growth mechanism to explore the possibility of kinetic frustration. In Figure 4a, the mean hexatic order plot is shown for samples with a few different volume ratios – 39:1, 19:1, 9:1, and 1:1, observed at different times and assembled with different SDS concentrations (i.e., different bond energy). We find the general trend of gradually decreasing $|\overline{\psi_6}|$ with increasing fraction of "impurity" (790 nm, red) particles. We also notice that the addition of impurities slows down the crystallization process. The sample with a higher SDS concentration (36.5 mM, $E_b \approx 6.1\, k_BT$) reaches its maximum crystalline state within about 90 min for all mixture ratios. In contrast, the sample with lower SDS concentration (34 mM, $E_b \approx 5.6\, k_BT$) crystallizes slowly, especially when impurities are added (compare the dark blue and cyan curves on Figure 4a). In this case, a monodisperse sample crystallizes with $|\overline{\psi_6}| = 0.77$ within only 3 hr; however, the 19:1 mixture ratio takes about 22 hr to obtain a similarly higher magnitude of $|\overline{\psi_6}| = 0.81$. It is expected that the average hexatic order for a sample with higher bond energy will be slightly smaller, because of the more frequent nucleation from different sites (the black curve is situated lower than the dark blue curve). Notably, we observe that the hexatic order of the 1:1 mixture is low for both SDS concentrations, regardless of the long observation time of up to 22 hr. Upon close examination of the assembled structures in the 19:1 sample ($E_b \approx 5.6\, k_BT$ after 22 hr), we notice that the ordered regions of the assembly consist mostly of the 700 nm particles (green) while the 790 nm particles (red) locate themselves in between the boundaries of different crystalline grains. All these observations indicate that the crystallization pathway is different in a suspension with large number of impurities compared to a monodisperse suspension.

Colloidal crystallization driven by short-ranged depletion interaction is known to follow a two-step nucleation pathway, distinct from the mechanism explained in the classical nucleation theory.[30] Savage et al. found that especially at a high area fraction, the assembly first forms amorphous clusters and grows in that state until a sudden increase in the hexatic order occurs resulting a crystalline state. The mechanism behind this two-step nucleation was explained by the reduction of the line tension in the intermediate amorphous phase that compensates for the lower bulk energy caused by the short interaction range. This is indeed what we observe in the crystallization pathway of the monodisperse sample (Figure 4b and 4c) – the assembly first grows in the amorphous state, and then stable crystallites start developing at about 40 min, which eventually grow and form boundaries between multiple crystalline grains (at t = 60 min, Figure 4c). However, in the binary sample, growth in this amorphous state continues for the entire timespan of the assembly, as depicted by the slow growth curve in Figure 4b and the snapshots in Figure 4c. The absence of two-step nucleation is binary mixtures is likely due to the size mismatch that causes a further reduction of the bulk energy in a binary simple compared to a monodisperse sample – as evident from the calculation of higher nucleation barrier in binary systems.[57] From the hexatic order plots during the early stage of crystal growth (0-60 min, Figure 4b), we observe the signature of a two-step growth mechanism only in the monodisperse suspension. Both the monodisperse and the binary mixture show a linear growth for the first 20 min, followed by a non-linear growth in the monodisperse sample and a continued linear growth in the binary sample (full field of view images and longer time growth characterization shown in Figure S10 and S11). We also examined different intermediate mixture ratios, such as 9:1, 5:1, and 3:1 (Figure S12) – although we observe the formation of stable grains via two-step nucleation in the 9:1 mixture sample, it becomes a rarer event when the fraction of the impurities increases in the 5:1 and 3:1 mixtures. From all the observations, it is reasonable to conclude that the second step of nucleation is much more likely to occur in a region where a critical number of particles with the same size can gather. Since it takes long time for this gathering to occur in the presence of the impurities, the 19:1 and 9:1 mixtures exhibit slower rates of growth in reaching their maximum $|\overline{\psi_6}|$ value (Figure 4a), and the 1:1 mixture remain frustrated for the entire timespan of observation (with a maximum $|\overline{\psi_6}|$ of only 0.63 after 22 hr, Figure 4a).

We verified that the major impact caused by the impurities is the two-step nucleation, and not the difference in deposition rate or the formation of second layers. The rate at which the particles attach to the surface, i.e., the deposition rate remains equal for both samples during the early stage of growth (Figure S13). The growth only slows down after 40 min for the binary sample due to the lack of available space for deposition. Therefore, we can conclude that the deposition rate is not the cause of kinetic frustration in the binary samples. Furthermore, the growth of second layers is only observed on top of a highly crystalline first layer, which acts a solid surface and induce a depletion interaction between the first layer and the second layer (Figure S14a). We do not observe any second layer formation in the 1:1 binary sample because of the highly amorphous first layer, indicating that the second layer cannot induce the kinetic frustration either.

Finally, we quantify the particle dynamics in the amorphous layer of the 1:1 binary mixture to identify any signature of arrested dynamics. The microscopic dynamics of the amorphous state was captured after the assembly continued for 80 min (Movie S1). While freely diffusing particles before assembly take 1 s to move 1 μm^2 (mean-squared displacement), the particles in the assembled layer of the binary sample take about 970 s to move only 0.1 μm^2 (Figure 5a). Additionally, we observe multiple partial vacancies in the assembly and cooperative particle movement adjacent to the locations of the partial vacancies. An example of the cooperative motion is presented and quantified in Figure 5c. Because of the remarkably short interaction range, particles fail to interact with each other across a partial vacancy and rearrange their positions locally due to their Brownian motions. These local movements result in continuous hopping of the vacancy locations (Figure 5c, Movie S1). Because of the high surface coverage, the fluctuating particles can support the relocation of their nearest neighbors, causing the cooperative movement observed in certain spots. Particle motion of this nature contributes to the overall arrested dynamics, which is a common feature observed near glass transition.[58,59] The four-point susceptibility, χ_4, calculated from a 50 μm x 30 μm region of the sample (Figure S15) shows a peak near 600 s (Figure 5b), demonstrating the signature of spatiotemporal heterogeneity in colloidal glasses.[47] Furthermore, when a stronger interaction potential is applied by increasing the concentration of the depletant micelles, the binary sample forms colloidal gels (Figure S16), transitioning from one nonequilibrium phase to another.

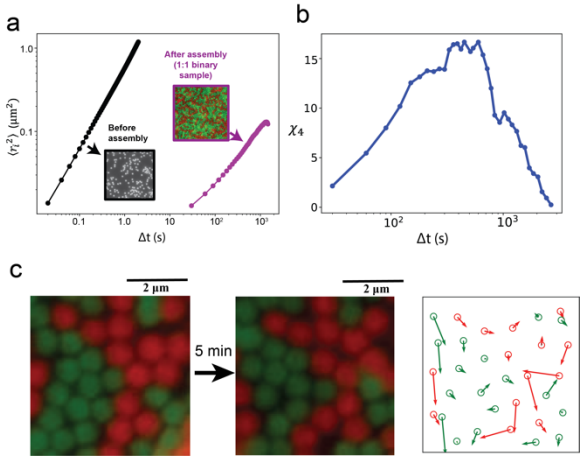

Figure 5 (a) Mean-squared displacement plots for particles before assembly (freely diffusing on a glass surface) and after assembly in a 1:1 binary mixture, showing significantly arrested dynamics. (b) The four-point susceptibility over time quantifies the temporal heterogeneity of the 1:1 binary sample. (c) Microscopic particle dynamics in an amorphous 1:1 binary mixture sample. Left: The snapshots of a self-assembled region taken in 5 min time interval show minute rearrangement of particle and vacancy positions. Right: A quiver plot quantifying and visualizing the displacements of all particles from (a) during the examined time interval. The cooperative motion of at least three groups of particles is observed as depicted by the groups of large arrows that point in the same direction.

Conclusions

We investigated the self-assembly of 2D binary colloidal crystals driven by short-ranged depletion interaction and in the presence of a marginal mismatch in the particle diameters. Our computational findings indicate that the minimum energy states maintain a high orientational order in a binary sample when the size ratio of the small to the large particle is 0.88. However, our experiments show a significant reduction (of about 18%) of the orientational order parameter in the 1:1 binary mixture compared to the monodisperse suspension. The order reduces gradually as the fraction of the impurity particles increases in the binary mixture. By carefully examining the crystallization kinetics, we find that the two-step nucleation mechanism that drives crystallization in the presence of short-ranged depletion interaction is responsible for the observed phenomenon. After growing in the amorphous state during the first step, the monodisperse sample enters the second nucleation step to rapidly form stable crystallites while the binary sample continues to grow in the amorphous state until the particle dynamics becomes arrested. These results have important implications for our general understanding of the mechanisms behind amorphous solid formation that originate from thermodynamic, kinetic, or topological conditions. Our findings on 2D binary assembly demonstrate that the frustration in growth kinetics can dominate over the topological frustration when a small mismatch in particle size is introduced. Leveraging this kinetic pathway of colloidal glass formation can stimulate progress in the fundamental studies on glass transitions [59–62] as well as applications focused on photonic glasses.[63–65] In addition, the binary mixtures with intermediate volume ratios (19:1 and 9:1) allow the nucleation of small crystallites whose growth is then inhibited by the presence of the impurities. Applications of this self-limiting formation of crystal grains could enable the design of polycrystalline and epitaxial colloidal materials [10,66–69] with precisely tuned optical and mechanical properties.

Author contributions

S.T.S performed the experiments, analyzed the experimental data, and prepared the manuscript. C.F. performed the Molecular Dynamics simulations. S.M. developed the computational methods used for image processing and data analysis. N.T. supervised the project and prepared the manuscript.

Conflicts of interest

There are no conflicts to declare.

Data availability

Data can be made available upon request.

Acknowledgements

We acknowledge the support from the National Science Foundation (NSF), award no. CBET – 2301692.

References

(1) Pusey, P. N.; van Megen, W. Phase Behaviour of Concentrated Suspensions of Nearly Hard Colloidal Spheres. *Nature* **1986**, *320* (6060), 340–342. https://doi.org/10.1038/320340a0.

(2) Li, B.; Zhou, D.; Han, Y. Assembly and Phase Transitions of Colloidal Crystals. *Nature Reviews Materials* **2016**, *1* (2). https://doi.org/10.1038/natrevmats.2015.11.

(3) Lu (陸述義), P. J.; Weitz, D. A. Colloidal Particles: Crystals, Glasses, and Gels. *Annual Review of Condensed Matter Physics* **2013**, *4* (1), 217–233. https://doi.org/10.1146/annurev-conmatphys-030212-184213.

(4) Manoharan, V. N. Colloidal Matter: Packing, Geometry, and Entropy. *Science* **2015**, *349* (6251). https://doi.org/10.1126/science.1253751.

(5) Anderson, V. J.; Lekkerkerker, H. N. W. Insights into Phase Transition Kinetics from Colloid Science. *Nature* **2002**, *416* (6883), 811–815. https://doi.org/10.1038/416811a.

(6) Bartlett, P.; Ottewill, R. H.; Pusey, P. N. Superlattice Formation in Binary Mixtures of Hard-Sphere Colloids. *Phys. Rev. Lett.* **1992**, *68* (25), 3801–3804. https://doi.org/10.1103/PhysRevLett.68.3801.

(7) Bartlett, P.; Ottewill, R. H.; Pusey, P. N. Freezing of Binary Mixtures of Colloidal Hard Spheres. *The Journal of Chemical Physics* **1990**, *93* (2), 1299–1312. https://doi.org/10.1063/1.459142.

(8) Sato, M. Two-Dimensional Binary Colloidal Crystals Formed by Particles with Two Different Sizes. *Sci Rep* **2022**, *12* (1), 12370. https://doi.org/10.1038/s41598-022-16806-y.

(9) Yu, J.; Yan, Q.; Shen, D. Co-Self-Assembly of Binary Colloidal Crystals at the Air−Water Interface. *ACS Appl. Mater. Interfaces* **2010**, *2* (7), 1922–1926. https://doi.org/10.1021/am100250c.

(10) Nozawa, J.; Uda, S.; Toyotama, A.; Yamanaka, J.; Niinomi, H.; Okada, J. Growth and One-Dimensional Heteroepitaxy of Binary Colloidal Crystals. *Crystal Growth & Design* **2020**, *20* (5), 3247–3256. https://doi.org/10.1021/acs.cgd.0c00078.

(11) Lopez-Godoy, S.; Díaz-Leyva, P.; Kozina, A. Self-Assembly in Binary Mixtures of Spherical Colloids. *Advances in Colloid and Interface Science* **2022**, *308*, 102748. https://doi.org/10.1016/j.cis.2022.102748.

(12) Yao, L. D.; Chen, H. Y.; Shi, Y.; Liang, Y.; Zhang, T. H. Synchronized Fractionation and Phase Separation in Binary Colloids. *Soft Matter* **2020**. https://doi.org/10.1039/D0SM00751J.

(13) Li, Y.; Royer, J. R.; Sun, J.; Ness, C. Impact of Granular Inclusions on the Phase Behavior of Colloidal Gels. *Soft Matter* **2023**, *19* (7), 1342–1347. https://doi.org/10.1039/D2SM01648F.

(14) Herlach, D. M. Colloids as Model Systems for Metals and Alloys: A Case Study of Crystallization. *Eur. Phys. J. Spec. Top.* **2014**, *223* (3), 591–608. https://doi.org/10.1140/epjst/e2014-02111-5.

(15) Hu, Y.; Lan, D.; Dai, G.; Jiang, H.; Duan, L.; Wei, B. Study on Crystallization Kinetics of Binary Alloys through Model Colloidal Mixtures. *Journal of Alloys and Compounds* **2010**, *504*, S243–S246. https://doi.org/10.1016/j.jallcom.2010.02.151.

(16) Diba, F. S.; Boden, A.; Thissen, H.; Bhave, M.; Kingshott, P.; Wang, P.-Y. Binary Colloidal Crystals (BCCs): Interactions, Fabrication, and Applications. *Advances in Colloid and Interface Science* **2018**, *261*, 102–127. https://doi.org/10.1016/j.cis.2018.08.005.

(17) Fernández-Rodríguez, M. Á.; Elnathan, R.; Ditcovski, R.; Grillo, F.; Conley, G. M.; Timpu, F.; Rauh, A.; Geisel, K.; Ellenbogen, T.; Grange, R.; Scheffold, F.; Karg, M.; Richtering, W.; Voelcker, N. H.; Isa, L. Tunable 2D Binary Colloidal Alloys for Soft Nanotemplating. *Nanoscale* **2018**, *10* (47), 22189–22195. https://doi.org/10.1039/C8NR07059H.

(18) Zhang, Z.; Yi, G.; Li, P.; Zhang, X.; Wan, Z.; Wang, X.; Zhang, C.; Zhang, Y. Recent Advances in Binary Colloidal Crystals for Photonics and Porous Material Fabrication. *J. Phys. Chem. B* **2021**, *125* (22), 6012–6022. https://doi.org/10.1021/acs.jpcb.1c03349.

(19) Shevchenko, E. V.; Talapin, D. V.; Kotov, N. A.; O'Brien, S.; Murray, C. B. Structural Diversity in Binary Nanoparticle Superlattices. *Nature* **2006**, *439* (7072), 55–59. https://doi.org/10.1038/nature04414.

(20) Wang, P.; Qiao, Q.; Zhu, Y.; Ouyang, M. Colloidal Binary Supracrystals with Tunable Structural Lattices. *J. Am. Chem. Soc.* **2018**, *140* (29), 9095–9098. https://doi.org/10.1021/jacs.8b05643.

(21) Leunissen, M. E.; Christova, C. G.; Hynninen, A.-P.; Royall, C. P.; Campbell, A. I.; Imhof, A.; Dijkstra, M.; van Roij, R.; van Blaaderen, A. Ionic Colloidal Crystals of Oppositely Charged Particles. *Nature* **2005**, *437* (7056), 235–240. https://doi.org/10.1038/nature03946.

(22) Rogers, W. B.; Shih, W. M.; Manoharan, V. N. Using DNA to Program the Self-Assembly of Colloidal Nanoparticles and Microparticles. *Nature Reviews Materials* **2016**, *1* (3), 16008. https://doi.org/10.1038/natrevmats.2016.8.

(23) Liu, M.; Zheng, X.; Grebe, V.; Pine, D. J.; Weck, M. Tunable Assembly of Hybrid Colloids Induced by Regioselective Depletion. *Nat. Mater.* **2020**. https://doi.org/10.1038/s41563-020-0744-2.

(24) Sacanna, S.; Irvine, W. T. M.; Chaikin, P. M.; Pine, D. J. Lock and Key Colloids. *Nature* **2010**, *464* (7288), 575–578. https://doi.org/10.1038/nature08906.

(25) Wang, Y.; Wang, Y.; Zheng, X.; Yi, G.-R.; Sacanna, S.; Pine, D. J.; Weck, M. Three-Dimensional Lock and Key Colloids. *J. Am. Chem. Soc.* **2014**, *136* (19), 6866–6869. https://doi.org/10.1021/ja502699p.

(26) Hinrichs, D.; Himstedt, R.; Dorfs, D. The Size-Selective Interaction of Key and Lock Nanocrystals Driven by Depletion Attraction at the Nanoscale. *Nanoscale* **2018**, *10* (21), 9899–9907. https://doi.org/10.1039/C8NR01893F.

(27) Park, S.; Hwang, H.; Kim, S.-H. Direct Determination of the Phase Diagram of a Depletion-Mediated Colloidal System. *J. Am. Chem. Soc.* **2022**, *144* (40), 18397–18405. https://doi.org/10.1021/jacs.2c06715.
(28) Parola, A.; Reatto, L. Depletion Interaction between Spheres of Unequal Size and Demixing in Binary Mixtures of Colloids. *Molecular Physics* **2015**, *113* (17–18), 2571–2582. https://doi.org/10.1080/00268976.2015.1046529.
(29) Onuh, G.; Harries, D.; Manor, O. Depletion-Induced Self-Assembly of Colloidal Particles on a Solid Substrate. *Langmuir* **2024**, *40* (16), 8554–8561. https://doi.org/10.1021/acs.langmuir.4c00186.
(30) Savage, J. R.; Dinsmore, A. D. Experimental Evidence for Two-Step Nucleation in Colloidal Crystallization. *Physical Review Letters* **2009**, *102* (19). https://doi.org/10.1103/PhysRevLett.102.198302.
(31) Tanjeem, N.; Wilkin, W. H.; Beller, D. A.; Rycroft, C. H.; Manoharan, V. N. Geometrical Frustration and Defect Formation in Growth of Colloidal Nanoparticle Crystals on a Cylinder: Implications for Assembly of Chiral Nanomaterials. *ACS Appl. Nano Mater.* **2021**, *4* (10), 10682–10691. https://doi.org/10.1021/acsanm.1c02126.
(32) Meng, G.; Paulose, J.; Nelson, D. R.; Manoharan, V. N. Elastic Instability of a Crystal Growing on a Curved Surface. *Science* **2014**, *343* (6171), 634–637. https://doi.org/10.1126/science.1244827.
(33) Rossi, L.; Sacanna, S.; Irvine, W. T. M.; Chaikin, P. M.; Pine, D. J.; Philipse, A. P. Cubic Crystals from Cubic Colloids. *Soft Matter* **2011**, *7* (9), 4139–4142. https://doi.org/10.1039/C0SM01246G.
(34) Baranov, D.; Fiore, A.; van Huis, M.; Giannini, C.; Falqui, A.; Lafont, U.; Zandbergen, H.; Zanella, M.; Cingolani, R.; Manna, L. Assembly of Colloidal Semiconductor Nanorods in Solution by Depletion Attraction. *Nano Lett.* **2010**, *10* (2), 743–749. https://doi.org/10.1021/nl903946n.
(35) Wu, G.; Cho, H.; Wood, D. A.; Dinsmore, A. D.; Yang, S. Confined Assemblies of Colloidal Particles with Soft Repulsive Interactions. *Journal of the American Chemical Society* **2017**, *139* (14), 5095–5101. https://doi.org/10.1021/jacs.6b12975.
(36) Ohnuki, R.; Sakai, M.; Takeoka, Y.; Yoshioka, S. Optical Characterization of the Photonic Ball as a Structurally Colored Pigment. *Langmuir* **2020**, *36* (20), 5579–5587. https://doi.org/10.1021/acs.langmuir.0c00736.
(37) Zhao, Y.; Shang, L.; Cheng, Y.; Gu, Z. Spherical Colloidal Photonic Crystals. *Acc. Chem. Res.* **2014**, *47* (12), 3632–3642. https://doi.org/10.1021/ar500317s.
(38) Ganapathy, R.; Buckley, M. R.; Gerbode, S. J.; Cohen, I. Direct Measurements of Island Growth and Step-Edge Barriers in Colloidal Epitaxy. *Science* **2010**, *327* (5964), 445–448. https://doi.org/10.1126/science.1179947.
(39) Zhou, J.; Duijneveldt, J. S. van; Vincent, B. Two-Stage Phase Separation in Ternary Colloid– Polymer Mixtures. *Physical Chemistry Chemical Physics* **2011**, *13* (1), 110–113. https://doi.org/10.1039/C0CP01523G.
(40) Kozina, A.; Sagawe, D.; Díaz-Leyva, P.; Bartsch, E.; Palberg, T. Polymer-Enforced Crystallization of a Eutectic Binary Hard Sphere Mixture. *Soft Matter* **2011**, *8* (3), 627–630. https://doi.org/10.1039/C1SM06699D.
(41) Bonham, J. A.; Faers, M. A.; van Duijneveldt, J. S. Binary and Ternary Mixtures of Microgel Particles, Hard Spheres and Non-Adsorbing Polymer in Non-Aqueous Solvents. *Colloids and Surfaces A: Physicochemical and Engineering Aspects* **2018**, *536*, 180–190. https://doi.org/10.1016/j.colsurfa.2017.07.022.
(42) Kozina, A.; Díaz-Leyva, P.; Palberg, T.; Bartsch, E. Crystallization Kinetics of Colloidal Binary Mixtures with Depletion Attraction. *Soft Matter* **2014**, *10* (47), 9523–9533. https://doi.org/10.1039/C4SM02193B.
(43) Toyotama, A.; Okuzono, T.; Yamanaka, J. Spontaneous Formation of Eutectic Crystal Structures in Binary and Ternary Charged Colloids Due to Depletion Attraction. *Sci Rep* **2016**, *6* (1), 23292. https://doi.org/10.1038/srep23292.
(44) Pandey, R.; C. Conrad, J. Dynamics of Confined Depletion Mixtures of Polymers and Bidispersed Colloids. *Soft Matter* **2013**, *9* (44), 10617–10626. https://doi.org/10.1039/C3SM51879E.
(45) Zhang, I.; Pinchaipat, R.; Wilding, N. B.; Faers, M. A.; Bartlett, P.; Evans, R.; Royall, C. P. Composition Inversion in Mixtures of Binary Colloids and Polymer. *The Journal of Chemical Physics* **2018**, *148* (18), 184902. https://doi.org/10.1063/1.5023393.
(46) Crocker, J. C.; Grier, D. G. Methods of Digital Video Microscopy for Colloidal Studies. *Journal of Colloid and Interface Science* **1996**, *179* (1), 298–310. https://doi.org/10.1006/jcis.1996.0217.
(47) Narumi, T.; Franklin, S. V.; Desmond, K. W.; Tokuyama, M.; Weeks, E. R. Spatial and Temporal Dynamical Heterogeneities Approaching the Binary Colloidal Glass Transition. *Soft Matter* **2011**, *7* (4), 1472–1482. https://doi.org/10.1039/C0SM00756K.
(48) Perry, R. W.; Holmes-Cerfon, M. C.; Brenner, M. P.; Manoharan, V. N. Two-Dimensional Clusters of Colloidal Spheres: Ground States, Excited States, and Structural Rearrangements. *Physical Review Letters* **2015**, *114* (22). https://doi.org/10.1103/PhysRevLett.114.228301.
(49) Asakura, S.; Oosawa, F. On Interaction between Two Bodies Immersed in a Solution of Macromolecules. *The Journal of Chemical Physics* **1954**, *22* (7), 1255–1256. https://doi.org/10.1063/1.1740347.
(50) Sun, J. H.; Zhang, G. H.; Plummer, A.; Martin, C.; Tanjeem, N.; Nelson, D. R.; Manoharan, V. N. Colloidal Crystallization on Cones. *Phys. Rev. Lett.* **2025**, *134* (1), 018201. https://doi.org/10.1103/PhysRevLett.134.018201.
(51) Dinsmore, A. D.; Yodh, A. G. Entropic Confinement of Colloidal Spheres in Corners on Silicon Substrates. *Langmuir* **1999**, *15* (2), 314–316. https://doi.org/10.1021/la981243w.
(52) Savage, J. R.; Blair, D. W.; Levine, A. J.; Guyer, R. A.; Dinsmore, A. D. Imaging the Sublimation Dynamics of Colloidal Crystallites. *Science* **2006**, *314* (5800), 795–798. https://doi.org/10.1126/science.1128649.
(53) Thompson, A. P.; Aktulga, H. M.; Berger, R.; Bolintineanu, D. S.; Brown, W. M.; Crozier, P. S.; in 't Veld, P. J.; Kohlmeyer, A.; Moore, S. G.; Nguyen, T. D.; Shan, R.; Stevens, M. J.; Tranchida, J.; Trott, C.; Plimpton, S. J. LAMMPS - a Flexible Simulation Tool for Particle-Based Materials Modeling at the Atomic, Meso, and Continuum Scales. *Computer Physics Communications* **2022**, *271*, 108171. https://doi.org/10.1016/j.cpc.2021.108171.
(54) Tanjeem, N.; Hall, D. M.; Minnis, M. B.; Hayward, R. C.; Grason, G. M. Focusing Frustration for Self-Limiting Assembly of Flexible, Curved Particles. *Phys. Rev. Research* **2022**, *4* (3), 033035. https://doi.org/10.1103/PhysRevResearch.4.033035.

(55) Iracki, T. D.; Beltran-Villegas, D. J.; Eichmann, S. L.; Bevan, M. A. Charged Micelle Depletion Attraction and Interfacial Colloidal Phase Behavior. *Langmuir* **2010**, *26* (24), 18710–18717. https://doi.org/10.1021/la103701k.

(56) Eckert, T.; Bartsch, E. Glass Transition Dynamics of Hard Sphere like Microgel Colloids with Short-Ranged Attractions. *J. Phys.: Condens. Matter* **2004**, *16* (42), S4937. https://doi.org/10.1088/0953-8984/16/42/011.

(57) Ganagalla, S. R.; Punnathanam, S. N. Free Energy Barriers for Homogeneous Crystal Nucleation in a Eutectic System of Binary Hard Spheres. *The Journal of Chemical Physics* **2013**, *138* (17), 174503. https://doi.org/10.1063/1.4802777.

(58) Yun, J.; Chun, B.; Jung, H. W.; Hyun, J. C. Emergence of Cooperative Particle Dynamics in Quasi-Two-Dimensional Glass-Forming Colloidal Suspensions. *Physics of Fluids* **2024**, *36* (1), 013311. https://doi.org/10.1063/5.0181383.

(59) Vivek, S.; Kelleher, C. P.; Chaikin, P. M.; Weeks, E. R. Long-Wavelength Fluctuations and the Glass Transition in Two Dimensions and Three Dimensions. *Proceedings of the National Academy of Sciences* **2017**, *114* (8), 1850–1855. https://doi.org/10.1073/pnas.1607226113.

(60) Hunter, G. L.; Weeks, E. R. The Physics of the Colloidal Glass Transition. *Rep. Prog. Phys.* **2012**, *75* (6), 066501. https://doi.org/10.1088/0034-4885/75/6/066501.

(61) Weeks, E. R.; Crocker, J. C.; Levitt, A. C.; Schofield, A.; Weitz, D. A. Three-Dimensional Direct Imaging of Structural Relaxation Near the Colloidal Glass Transition. *Science* **2000**, *287* (5453), 627–631. https://doi.org/10.1126/science.287.5453.627.

(62) Lynch, J. M.; Cianci, G. C.; Weeks, E. R. Dynamics and Structure of an Aging Binary Colloidal Glass. *Phys. Rev. E* **2008**, *78* (3), 031410. https://doi.org/10.1103/PhysRevE.78.031410.

(63) Demirörs, A. F.; Poloni, E.; Chiesa, M.; Bargardi, F. L.; Binelli, M. R.; Woigk, W.; de Castro, L. D. C.; Kleger, N.; Coulter, F. B.; Sicher, A.; Galinski, H.; Scheffold, F.; Studart, A. R. Three-Dimensional Printing of Photonic Colloidal Glasses into Objects with Isotropic Structural Color. *Nat Commun* **2022**, *13* (1), 4397. https://doi.org/10.1038/s41467-022-32060-2.

(64) Romanov, S. G.; Orlov, S.; Ploss, D.; Weiss, C. K.; Vogel, N.; Peschel, U. Engineered Disorder and Light Propagation in a Planar Photonic Glass. *Sci Rep* **2016**, *6* (1), 27264. https://doi.org/10.1038/srep27264.

(65) Shang, G.; Eich, M.; Petrov, A. Photonic Glass Based Structural Color. *APL Photonics* **2020**, *5* (6), 060901. https://doi.org/10.1063/5.0006203.

(66) Lavergne, F. A.; Diana, S.; Aarts, D. G. A. L.; Dullens, R. P. A. Equilibrium Grain Boundary Segregation and Clustering of Impurities in Colloidal Polycrystalline Monolayers. *Langmuir* **2016**, *32* (48), 12716–12724. https://doi.org/10.1021/acs.langmuir.6b02683.

(67) Hutchinson, J. D.; Dullens, R. P. A. Grain Rotation in Impurity-Doped Two-Dimensional Colloidal Polycrystals. *Phys. Rev. Mater.* **2024**, *8* (7), 075603. https://doi.org/10.1103/PhysRevMaterials.8.075603.

(68) Nozawa, J.; Uda, S.; Niinomi, H.; Okada, J.; Fujiwara, K. Heteroepitaxial Growth of Colloidal Crystals: Dependence of the Growth Mode on the Interparticle Interactions and Lattice Spacing. *J. Phys. Chem. Lett.* **2022**, *13* (30), 6995–7000. https://doi.org/10.1021/acs.jpclett.2c01707.

(69) Yang, S.; Kim, Y. G.; Park, S.; Kim, S.-H. Structural Color Mixing in Microcapsules through Exclusive Crystallization of Binary and Ternary Colloids. *Advanced Materials* **2023**, *35* (38), 2302750. https://doi.org/10.1002/adma.202302750.

The data that support the findings of this study are available from the corresponding author, Nabila Tanjeem, upon request.